crystals

MDPI

Article

Thickness Study of Ga_2O_3 Barrier Layer in p-Si/n-MgZnO:Er/Ga_2O_3/ZnO:In Diode

Shih-Wei Ying [1], Shou-Yen Chao [2], Ming-Chang Shih [1], Chien-Jung Huang [3] and Wen-How Lan [1,*]

[1] Department of Electrical Engineering, National University of Kaohsiung, Kaohsiung 81148, Taiwan
[2] Department of Electronic Engineering, Minghsin University of Science and Technology, Hsinchu 30401, Taiwan
[3] Department of Applied Physics, National University of Kaohsiung, Kaohsiung 81148, Taiwan
* Correspondence: whlan@nuk.edu.tw

Abstract: The p-Si/n-MgZnO:Er/Ga_2O_3/ZnO:In diodes with different Ga_2O_3 thicknesses were fabricated through spray pyrolysis deposition at 450 °C with aqueous solutions containing magnesium nitrate, zinc acetate, erbium acetate, gallium nitrate, and indium nitrate precursors. The effects of Ga_2O_3 layer thickness on the diode properties were investigated. For the deposited films, a combined tiny hexagonal slices and small blocks surface morphology was characterized by scanning electron microscopy for all samples. Diodes were formed after In and Ag deposition on the back side and top side, respectively. The current-voltage characteristics and luminescence spectra are studied. With the increasing of Ga_2O_3 thickness, the diode forward bias resistance increases while the reverse biased dark current shows the decrease-increase characters. The Er ion corresponded green light emission was characterized for the diode under reverse biased breakdown condition. The increased luminescent intensity with low turn-on current behaviors was characterized by the diode with a Ga_2O_3 thickness of 4.9 nm. With the diode electrical and luminescence analysis, the effect of the Ga_2O_3 barrier layer on the diode was discussed. The Ga_2O_3 barrier layer improves performance for rare earth-related light-emitting devices.

Keywords: gallium oxide; magnesium zinc oxide; erbium; diode

Citation: Ying, S.-W.; Chao, S.-Y.; Shih, M.-C.; Huang, C.-J.; Lan, W.-H. Thickness Study of Ga_2O_3 Barrier Layer in p-Si/n-MgZnO:Er/Ga_2O_3/ZnO:In Diode. *Crystals* **2023**, *13*, 275. https://doi.org/10.3390/cryst13020275

Academic Editor: Robert F. Klie

Received: 21 November 2022
Revised: 31 January 2023
Accepted: 3 February 2023
Published: 5 February 2023

Copyright: © 2023 by the authors. Licensee MDPI, Basel, Switzerland. This article is an open access article distributed under the terms and conditions of the Creative Commons Attribution (CC BY) license (https://creativecommons.org/licenses/by/4.0/).

1. Introduction

In the past decade, zinc oxide (ZnO) and its related materials have got certain interests in electronic and optoelectronic applications. Devices such as field effect transistors [1], photodiode [2], laser [3], and light-emitting diodes (LEDs) [4] have been reported with promising performance. For a non-toxic material with high chemical and thermal resistance properties, some interest arises in ZnO based on its large exciton binding energy (60 meV). This high binding energy character suggests ZnO is a favorable light-emitting device. Meanwhile, Si is the most important semiconductor material. The integrated Si and ZnO-based device has great attraction for further device development. One of these kinds of photonic devices, the silicon (Si) substrate integrated erbium (Er) doped ZnO/MgZnO light emitting diode [5,6], shows the promising Si-based photonic devices for communication as the Er-related green emission matches the low loss band of PMMA (polymethyl methacrylate) core optical fiber [7]. For this rare-earth element doped light emitting diode, a high reverse bias condition is generally required for ensuring high energy carrier generation and energy transformation to Er-related energy states after the impact excitation mechanism [5]. The light emission was observed by the relaxation process from the excited state to the ground state of the rare-earth element. For the diode under high electric field operation before light emission, certain currents can be characterized. A photonic device with a high turn-on current before light emission, thus, exhibits poor performance.

For photonic devices, carrier confinement is important for controlling the recombination process. The carrier blocking layer can, thus, be embedded in the structure for

device performance, improving InGaN LED [8], and Perovskite solar cells [9]. For the Si substrate-based device, the high band gap SiOx formed on the Si surface by the thermal process exhibits a good carrier-blocking character on the bottom side of the luminescent host. The reduced turn-on current before light emission was characterized by this introduced bottom-side SiOx blocking layer in the diode structure [10].

For efficient carrier blocking in ZnO, some wide bandgap materials such as AlN [11], MgZnO [12], and Ga_2O_3 [13] can be taken as the barrier layer. For these wide bandgap materials, Ga_2O_3, which shows high breakdown voltage characteristics [14] with a wide bandgap of 4.7–5 eV, presents a promising property for barrier material. Although there are studies on the effects of the barrier layer on ZnO-based photonic devices [15], fewer studies can be found on the effect of the barrier layer on the top side of the luminescent host.

A variety of film deposition techniques, such as molecular beam epitaxy method, chemical vapor deposition method, sputtering technique, sol-gel technique, and spray pyrolysis method, etc., has been developed for preparing the ZnO-based devices. Among them, the non-vacuumed spray pyrolysis method has got more interest owing to its inexpensive and easy scale-up abilities. In our previous work, we report the active layer thickness effect of the MgZnO:Er diode by spray pyrolysis [16]. In this work, the Ga_2O_3 barrier layer was introduced on the top side of the MgZnO:Er host in the diode structure. The effects of Ga_2O_3 thickness on the diode current–voltage and luminescence properties were studied. The optimized Ga_2O_3 thickness for the reductions of the reverse biased leakage current and the turn-on current before light emission were characterized, and the mechanism was discussed.

2. Materials and Methods

The device structures p-Si/MgZnO:Er/Ga_2O_3/ZnO:In were prepared by spray pyrolysis at 450 °C on the p-Si substrate. The Si substrate was cleaned with acetone, rinsed in de-ionized (DI) water, dried by N_2 gas, dipped in 5% HF aqueous solution, rinsed in DI water, and dried by N_2 gas. The substrate was then transferred to the deposition chamber. A thin SiOx of about 3 nm was formed on the surface underwater mist. Three aqueous solutions were prepared for the sequential film deposition. The zinc acetate dehydrate ($Zn(CH_3COO)_2 \cdot 2H_2O$, 0.2 M), magnesium nitrate hexahydrate ($Mg(NO_3)_2 \cdot 6H_2O$) 0.05 M (Mg/Zn = 25%), and erbium acetate hydrate ($Er(CH_3COO)_3 \cdot 4H_2O$) 0.01 M (Er/Zn = 5%) aqueous was prepared in forming MgZnO:Er. The gallium nitrate octahydrate ($Ga(NO_3)_3 \cdot 8H_2O$) aqueous (0.1 M) with glucose was prepared for the deposition of Ga_2O_3. The zinc acetate dehydrate (0.2 M) and indium nitrate hydrate ($In(NO_3)_3 \cdot 5H_2O$) 0.01 M aqueous (In/Zn = 5%) were prepared for the deposition of the ZnO:In layer. The thickness of the MgZnO:Er and ZnO:In were about 300 nm and 100 nm, respectively. The backside in contact was the formation by the thermal deposition process. The front side Ag contact with a diameter of 0.6 mm was formed with a metal mask by sputter. Diode samples with different Ga_2O_3 deposition times of 1 min, 3 min, and 7 min were prepared, and the sample codes were AT1, AT3, and AT7, respectively. For comparison, the pn diode without the Ga_2O_3 layer was also prepared with sample code AT0. On the other hand, Ga_2O_3 films with deposition times of 1 min, 3 min, and 7 min were deposited on the p-Si substrate also under the same parameters described above. After the same metallization process, the MOS structure (p-Si/Ga_2O_3/Ag) was formed. The sample codes were AP1, AP3, and AP7, respectively. Moreover, Ga_2O_3 films were prepared with a deposition time of 20 min on quartz and Si substrates, respectively, for film optical and elements analysis. On the other hand, unintentionally doped ZnO and MgZnO were deposited at 450 °C on a Si substrate with the same deposition parameters for photoluminescence analysis.

The surface morphologies and the elements of the films were characterized by scanning electron microscopy (SEM, Hitachi S4300) with EDS (Energy-dispersive X-ray spectroscopy). The element contents of the film were achieved by XPS analysis (ECSALAB XI^+). The MOS capacitance–voltage (C-V) characteristics were examined by an impedance analyzer (Agilent 4294A) at 100 kHz. The photoluminescence (PL) spectrum was achieved by

an optical system with the spectrometer (Ocean Optics HR2000+) and HeCd laser with emission wavelength 325 nm mainly. The diode current–voltage (I–V), luminescence spectrum, and optical property were characterized by a source meter (Keithley 2400) and an optical fiber integrated spectrometer (Ocean Optics HR2000+).

3. Results and Discussion

Figure 1 shows the XPS spectra of (a) O 1s and (b) Ga $2p_{3/2}$ for sample SP20. In Figure 1a, the O 1s spectra show the three oxygen signals with binding energy 531.1 eV, 533.5 eV, and 535.1 eV, respectively. The peak at 531.1 eV is ascribed to lattice oxygen in Ga–O bonding [17]. The peak at 532.8 eV is attributed to the C-related O state [18] and or O–H bonds [19]. For the film prepared by mist-CVD, carbon and hydrogen species in the precursor may be incorporated into the film in the deposition process. The peak at 535.1 eV shows the characteristic peaks of O in β-Ga_2O_3 [20]. In Figure 1b, the Ga $2p_{3/2}$ consists of three components at 1122.2 eV, 1119.9 eV, and 1117.8 eV were observed. The peaks located at 1122.2 eV and 1119.9 eV are known to Ga in Ga-O bonding for β-Ga_2O_3 structure [20] and α-Ga_2O_3 structure [21], respectively. The peak at 1117.8 eV was attributed to Ga 1+ oxidation state in Ga_2O bonding and may be formed in the interface through the decomposition of the Ga_2O_3 source [22,23]. As the calculated core state binding energy difference for the same atom in the primitive unit cell is small, the broadness of the binding energy in XPS may originate from the instrumental broadening and the carrier lifetime broadening of the excitations [24].

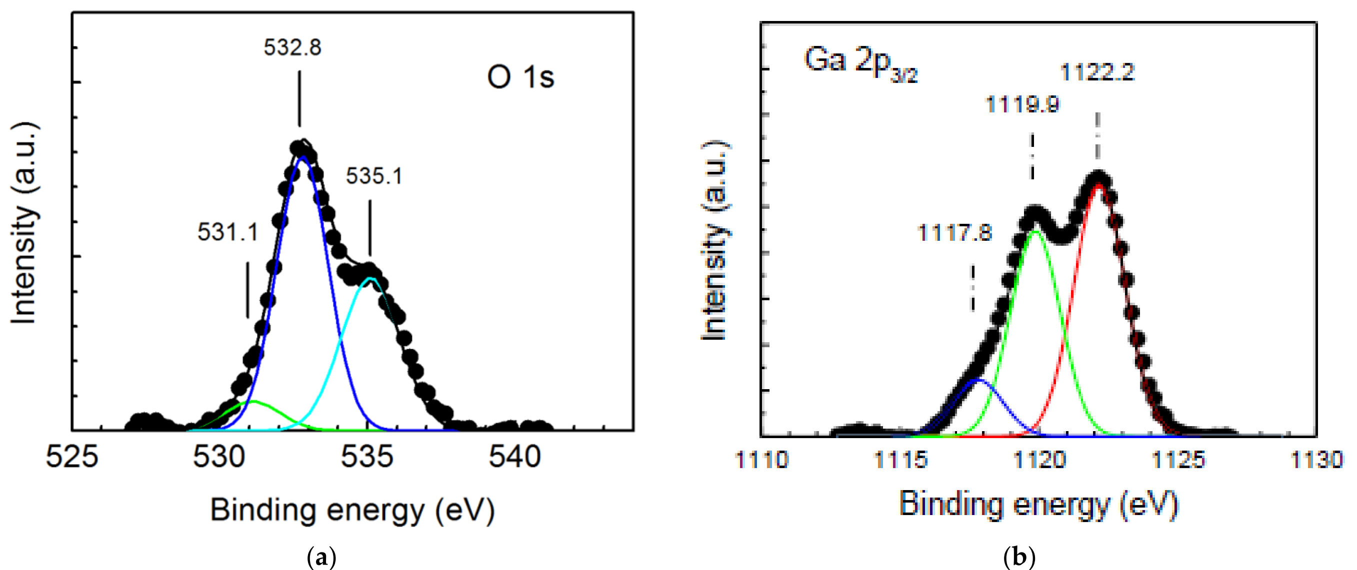

Figure 1. The XPS spectra of (**a**) O 1s and (**b**) Ga $2p_{3/2}$ for sample SP20.

Figure 2 shows the spectral dependences of the absorption coefficient for (a) Ga_2O_3 thin film and (b) the quartz glass substrate. The inset shows the corresponding Tauc plot of Ga_2O_3. The low absorption coefficient of the quartz substrate in the spectrum was characterized. For the prepared Ga_2O_3 film, the absorption coefficient increased sternly with a wavelength less than 280 nm region. The Tauc plot for Ga_2O_3 was shown in the inset with photon energy hν. The optical bandgap extracted from the linear interpolation in the shaded region around 4.70–4.84 eV can be obtained. In the following band diagram alignment, the bandgap value 4.77 eV was used from the mean value of 4.70 eV and 4.84 eV for the prepared Ga_2O_3. This bandgap value is between the reported bandgap value for α-Ga_2O_3 (5 eV) [21] and β-Ga_2O_3 (4.69–4.71 eV) [25].

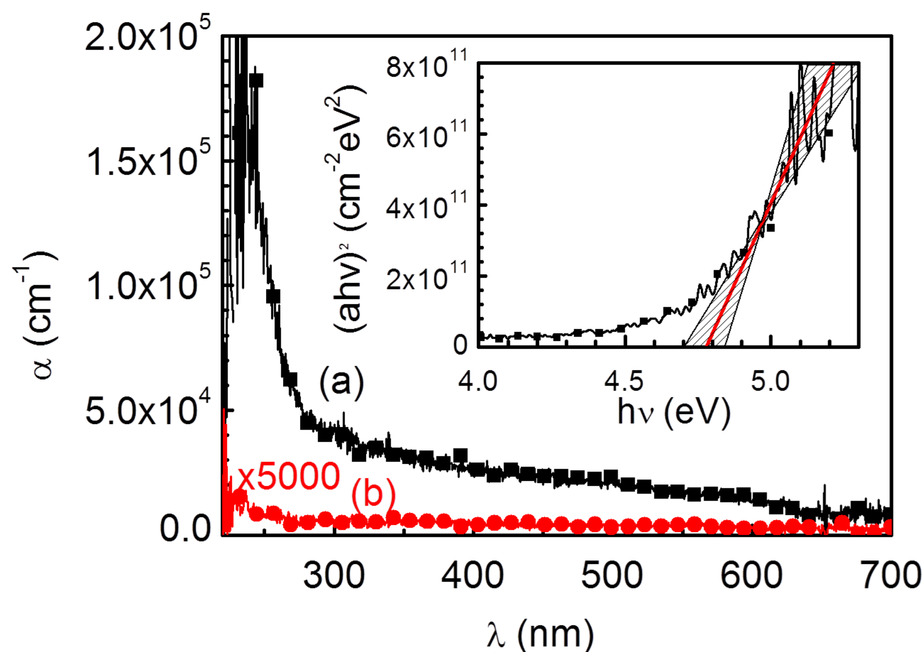

Figure 2. Spectral dependences of the absorption coefficient for (**a**) Ga_2O_3 thin film and (**b**) the quartz glass substrate. The inset shows the corresponding Tauc plot of Ga_2O_3.

For the crystalline and composition evaluation, the unintentionally doped ZnO and MgZnO were deposited on a Si substrate with the same deposition parameters for photoluminescence analysis. Figure 3 shows the room temperature PL spectrum with photon energy E(eV) for the unintentionally doped ZnO and MgZnO films. Emissions in both the ultraviolet (UV) band (E > 3.1 eV) and visible (VIS) band (1.8 eV < E < 3.1 eV) in the spectrum for both ZnO and MgZnO samples can be observed. For ZnO, the characteristic near band edge (NBE) signal with peak energy 3.30 eV with a corresponding wavelength of 376 nm was observed. This is an attribute of carrier transitions from the free exciton (FX) level to the valence band (VB) [26]. The sub-peak at 3.23 eV and 3.16 eV, which shows the energy state with less 72 meV and 144 meV than the NBE signal, respectively, is the first and second longitudinal optic (LO) phonon replica of the NBE signal [27]. For the free exciton binding energy 60 meV [28], the bandgap of ZnO is known to be 3.36 eV.

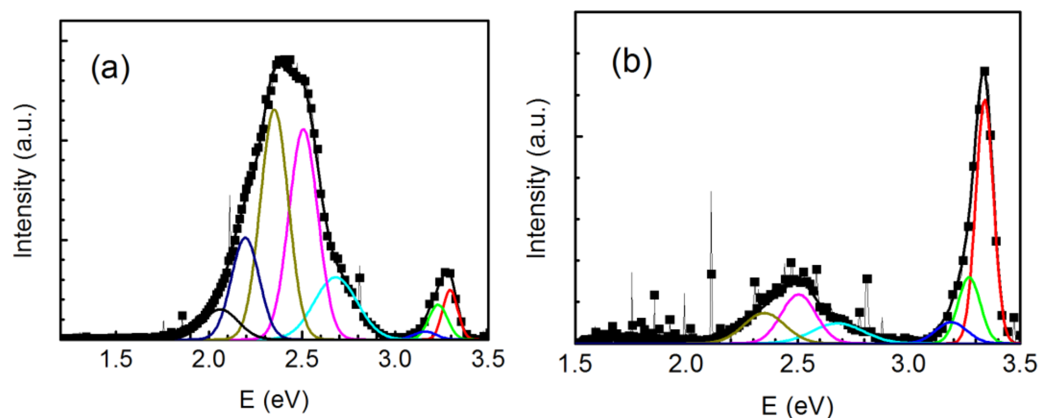

Figure 3. The photoluminescence spectrum for (**a**) ZnO and (**b**) MgZnO at room temperature.

For the VIS band emissions, broad emissions around 1.8 eV–2.9 eV with corresponding wavelengths 430 nm–690 nm [29,30] were observed. The emissions can be fitted to several peaks, as shown in the figure. The fitted emissions can be related to the Zn interstitial (Zn_i) state (3.15 eV, 390 nm) [30], zinc vacancy (V_{Zn}) state (2.5 eV, 496 nm) [31], oxygen vacancy (V_O^+) [30] and oxygen antisite (O_{Zn}) state [32] (2.34 eV, 530 nm), the doubly charged oxygen

vacancy (V_O^{++}) state (2.19 eV, 566 nm) [32], and Zn interstitial to oxygen interstitial (Zni-Oi) state (2.06 eV, 602 nm) [33].

For the MgZnO film, as shown in Figure 3b, a blue shift in NBE emissions and the intensity reduction in VIS emissions was observed. The fitted emission in the UV band is attributed to NBE emission (3.34 eV, 371 nm), and its first phonon replica (3.27 eV, 379 nm) and the second phonon replica (3.20 eV, 388 nm). After considering the same exciton binding energy as that of ZnO, the bandgap of MgZnO can be achieved as 3.4 eV. The emissions in the VIS band were fitted with peaks similar to that in ZnO, as the peak broadening is larger than the wavelength blue shift in the NBE signal. For MgZnO, only three fitted PL peaks in the VIS band can be observed. These were attributed to the Zn interstitial (Zn_i) state (3.15 eV), zinc vacancy (V_{Zn}) state (2.5 eV), and oxygen vacancy (V_O^{+}) and oxygen antisite (O_{Zn}) state (2.34 eV). The intensity depression of these three residue emissions and emission elimination of V_O^{++} state (2.19 eV) and Zni-Oi transmission (2.06 eV) reveals the defects reduction [24] for the prepared MgZnO. With the inhibition of these O-related and Zn-related defects, MgZnO can be served as a good host material for rare-earth doping. Moreover, with the energy difference for the near band edge signal for ZnO and MgZnO, the Mg content in the film was estimated to be 3% ($Mg_{0.03}Zn_{0.97}O$) [34].

Figure 4 exhibits the C−V characteristics for the sample AP1, AP3, and AP7, respectively. The flat-down-flat character in the CV curve with the increase in bias voltage can be observed for all samples. This corresponded to carrier accumulation, depletion, and inversion conditions in MOS (p-Si/Ga_2O_3/Ag) structure. The capacitance in the accumulation condition shows the oxide capacitance. The capacitance in inversion shows reduced capacitance after considering the oxide capacitance and semiconductor junction capacitance. For samples AP1, AP3, and AP7, the accumulation condition occurred with bias voltage excess −0.3 V, and the measured capacitance corresponded to oxide capacitance (Cox). The decreased Cox for samples AP1 to AP7 can be observed in Figure 4. This shows the increased oxide thickness of the MOS structure with the increased deposition time. With considering the electrode area, relative dielectric constant 10.2 [14], and the oxide capacitance, the effective oxide thickness d was achieved. The thickness was 2.6 nm, 4.9 nm, and 7.7 nm for samples AP1, AP3, and AP7, respectively. The result is shown in the inset of Figure 4.

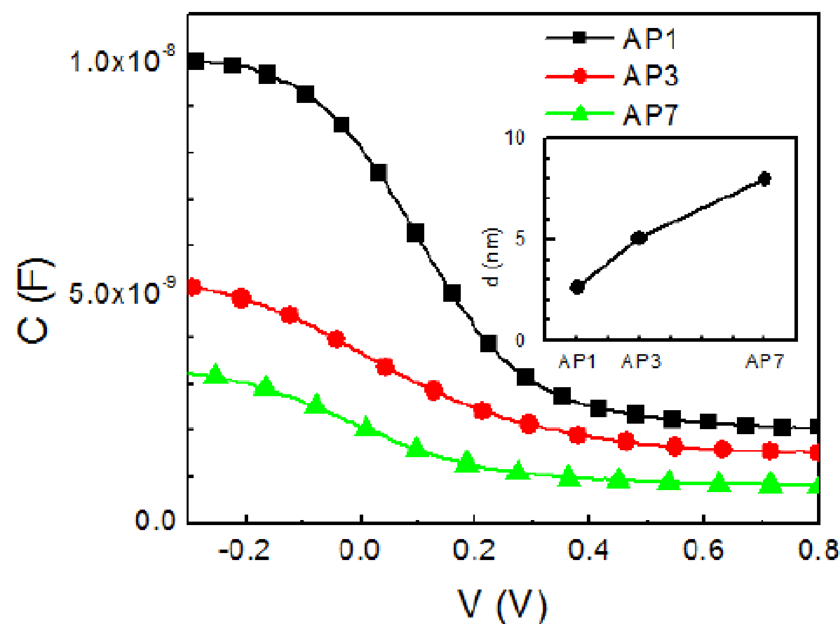

Figure 4. The capacitance−voltage (C−V) characteristics of Ga_2O_3 MOS AP1, AP3, and AP7. The effect of oxide thickness d for each sample was shown in the inset.

Figure 5 shows the surface morphology of samples (a) AT0, (b) AT1, (c) AT3, and (d) AT7. The surface morphology with combined hexagonal flakes and small rods was observed for the AT0 sample. This surface expresses a morphology originating from the spray pyrolysis process with magnesium nitrate hexahydrate and zinc acetate dehydrate precursors. With the introduced thin Ga_2O_3 layer between MgZnO:Er and ZnO:In layer, similar morphology for samples AT1, AT3, and AT7 can be observed.

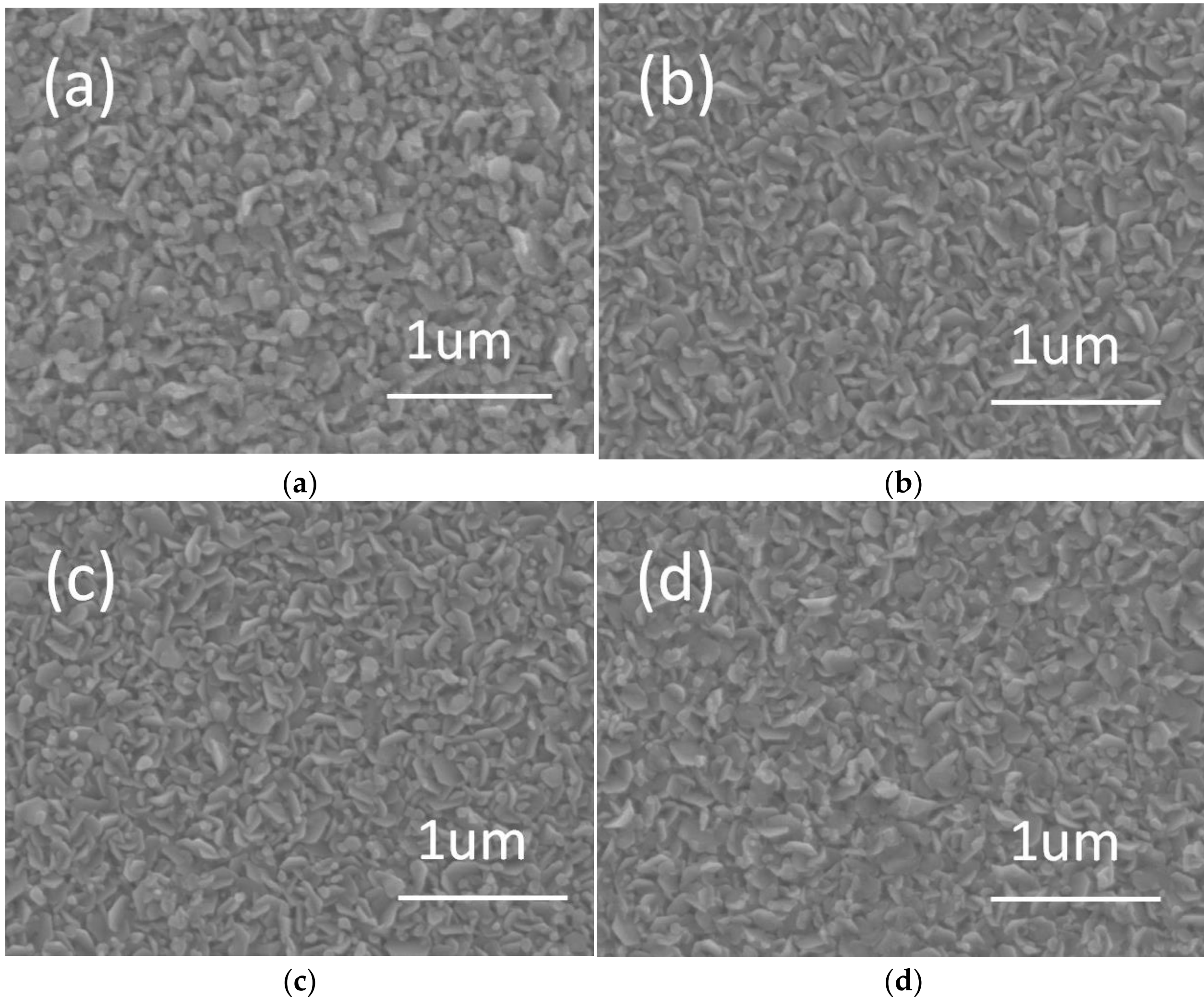

(**a**) (**b**) (**c**) (**d**)

Figure 5. Surface morphology of samples (**a**)AT0, (**b**) AT1, (**c**) AT3, and (**d**) AT7.

Figure 6 shows the current−voltage (I−V) characteristics of samples AT0, AT1, AT3, and AT7 measured at room temperature. In the forward bias region, a little increase in the turn-on voltage with the introduced and increased Ga_2O_3 thickness can be observed for samples AT0 to AT7. For a pn diode considering the series resistance, the ideality factor η and series resistance Rs can be extracted from the IdV/dI−I plot in forward bias condition as [35]

$$I\frac{dV}{dI} = I \times Rs + \eta\frac{k_B T}{q} \quad (1)$$

while k_B, T, and q are Boltzmann constant, diode temperature, and the elementary charge, respectively. The extracted ideality η and series resistance Rs for samples AT0, AT1, AT3, and AT7 were listed in Table 1. The increased Rs of AT1 compared to that of AT0 was characterized. The bandgap of Ga_2O_3 around 4.8 eV is higher than that of the MgZnO and ZnO layer in this study. For AT1 to AT7, the increased Rs due to the increased Ga_2O_3 layer thickness was observed. The increased Rs for AT1 is owing to the occurred barrier

height of the Ga_2O_3 layer and the adjacent layers. A little ideality factor difference due to carrier transport variant with introduced Ga_2O_3 layer was characterized. The increased ideality factor η reveals the degraded crystalline, which may be caused by the coupled defects [36] increase with the increasing of Ga_2O_3 thickness. In the reverse bias region, the breakdown occurred for all samples with reverse bias excessed −6.2 V. The reduced steep I–V character in the breakdown region was observed for the diode with the increased Ga_2O_3 thickness. This is due to the increased diode series resistance *Rs* originating from the introduced Ga_2O_3 layer. The fine plot around reverse bias 0 to −2 V was shown in the inset. The inhibited reverse-biased dark current before breakdown was characterized for samples AT1 and AT3 compared to that of AT0. Yet, the increased dark current for sample AT7 with a thick Ga_2O_3 layer can also be observed. This reveals the enhanced carrier recombination character and may be originated from the increased defect states for the thick Ga_2O_3 sample AT7.

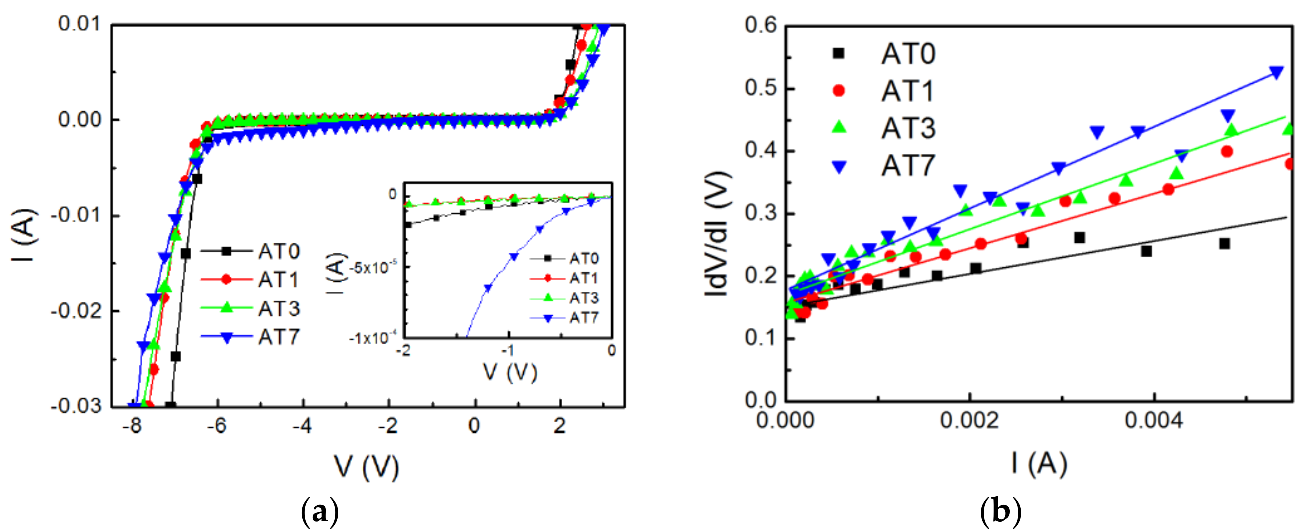

Figure 6. (**a**) The current−voltage (I−V) characteristics of samples AT0, AT1, AT3, and AT7 measured at room temperature. The insect shows the fine-scale in 0 to −2 V region. (**b**) The IdV/dI−I plot for extracting the diode ideality factor and series resistance.

Table 1. The diode ideality factor (n) and series resistance (*Rs*) of the sample AT0, AT1, AT3, and AT7.

Sample	η	*Rs* (Ω)
AT0	6.4	22.4
AT1	6.3	44.2
AT3	6.9	50.6
AT7	7.0	60.1

The diode luminescent was observed for the diode under reverse bias in the breakdown condition. Figure 7 shows the luminescent intensity (L) to reverse biased injection current ($I_{inj.}$) relations for diode AT0, AT1, AT3, and AT7. For sample AT0, no spectral response for injection current less than 9 mA. A little spectrum response was observed while the injection current reached 20 mA. An obvious green light emission can be observed with an injection current in excess of 30 mA. For sample AT1, a little spectral response can be observed while applying a 1 mA injection current on the diode. A green light emission can be observed with a higher injection current by the naked eye. For sample AT3, the spectral response and obvious green light emission were characterized with a 1 mA injection current. For the thick Ga_2O_3 sample AT7, a high turn-on current was characterized, and green light emission was observed with a 10 mA injection current.

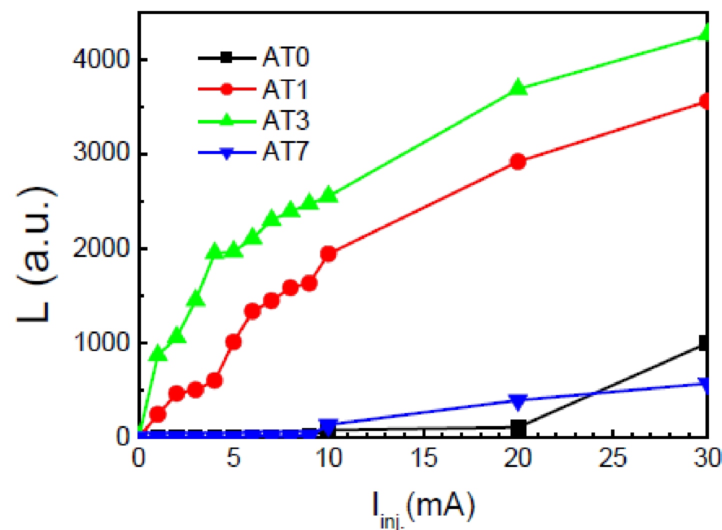

Figure 7. The luminescent intensity (L)-injection current (Iinj.) characteristics for diode AT0, AT1, AT3, and AT7.

The luminescent spectrum of each sample under different reverse-biased injection currents is shown in Figure 8. The characterized emission spectrum around 533 nm and 553 nm was correlated to the Er^{3+} $^2H_{11/2}$→$^4I_{15/2}$ and $^4S_{3/2}$→$^4I_{15/2}$ energy state transitions [5], respectively. For samples AT0, AT1, and AT3, similar spectrum distribution for the two characteristic emissions was observed. Yet, the emission spectrum of sample AT7 is far from that of sample AT0 to AT3. In this rare earth-doped optoelectronic device, the characteristic emission is from the core of rare earth elements, while the spectral distribution is controlled by the host material. For samples AT0 to AT3, similar spectra reveal similar crystalline of the MgZnO:Er host. Varied emission spectra for sample AT7 shows the different crystalline. As a high turn-on current and a large dark current were characterized for sample AT7, reduced crystalline was expected for this sample. This reduced crystalline region may occur beneath the Ga_2O_3 in the deposition process while considering the diode structure.

For the optical pumped rare earth element doped optoelectronic device, the luminescence for upconversion and downconversion can be distinguished. The luminescence mechanism was characterized by the luminescent intensity (L) to pumping power (P) relations with different power orders [37]. The slope change of the down-conversion luminescence intensity changes from power order n = 1 (~ P^1) at low pumping power toward power order n = 0.5 (~ $P^{0.5}$) at high pumping power. The slope change of the up-conversion luminescence with more than one photon mechanism shows the high power order quantity (n > 1).

Figure 9 shows the double logarithmic plot for the two characteristic emission intensities L_{533nm} and L_{553nm} for samples AT0, AT1, AT3, and AT7 to injection current ($I_{inj.}$) measured at room temperature. The power order n of emission intensity to injection current shows two branches, basically. For AT1, the intensity L to injection current ($I_{inj.}$) shows n = 1 (L ~ $I_{inj.}^{1}$) with low injection current (<5 mA) and n = 0.5 (L ~ $I_{inj.}^{0.5}$) with injection current excess 10 mA. The L-$I_{inj.}$ relation with order n = 1 shows the direct pumping-relaxation mechanism, which was the same as that in the downconversion luminescence by low-power optical pumping. With increased injection current, the carriers at the excited state may take the impact excitation energy again to higher energy states and or the defect states of the host material. High energy carriers, thus, back to their initial state after the non-radiative depopulation mechanisms [37]. Few photons can be generated by this process. The reduced injection current power order (n < 1) for high injection current can be expected. For AT3, the emission intensity shows the injection current to the power order 0.5 (L ~ $I_{inj.}^{0.5}$). This shows the high current injection condition for AT3. For the injection current 10 mA, both AT1 and AT3 show the same power order of 0.5. Thus the

power order n = 1 for AT7 reveals that some measured current takes less contribution to photon generation as in the low injection condition. The low emission intensity in the power order n = 1 region, thus, can be realized. Moreover, it was known that the variation of intensity ratio for the rare earth element's characteristic emissions might be referred to as the characteristic temperature [38]. As both intensities, L_{533nm} and L_{553nm}, in Figure 9 have the same trend for each sample, the intensity ratio (L_{533nm}/L_{553nm}) remains constant with the increase in $I_{inj.}$ for all samples. The temperature variation in this operation range may be less.

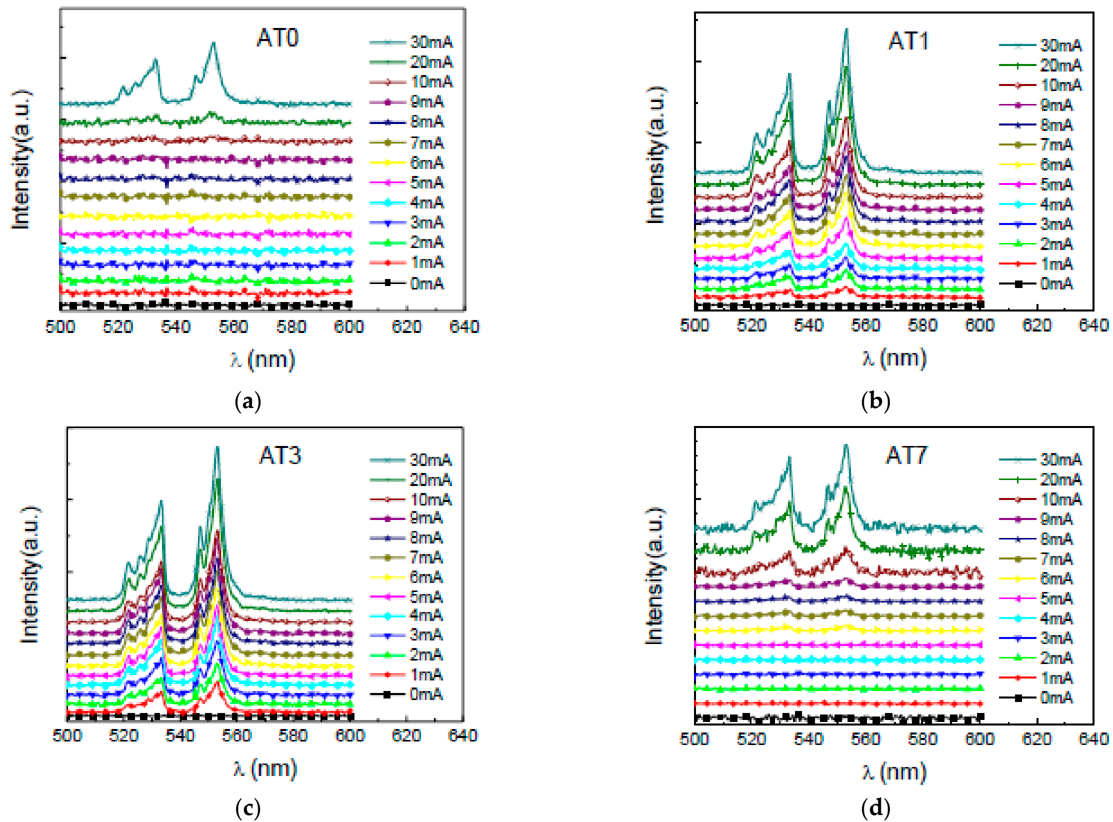

Figure 8. The luminescent spectrum of samples (**a**) AT0, (**b**) AT1, (**c**) AT3, and (**d**) AT7 under different reverse-biased injection current levels.

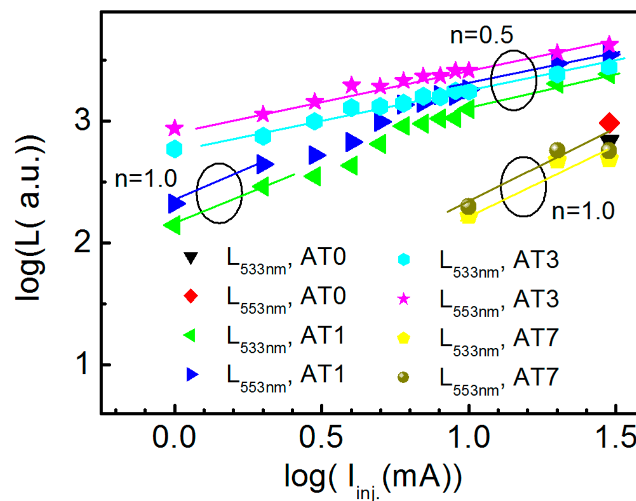

Figure 9. The log(L)) to log(Iinj.) plot with two characteristic emissions Er^{3+} $2H_{11/2}{\rightarrow}4I_{15/2}$ (wavelength 533 nm) and $4S_{3/2}{\rightarrow}4I_{15/2}$ (wavelength 553 nm) for sample AT0, AT1, AT3 and AT7 measured at room temperature with different injection current level ($I_{inj.}$).

The schematic band diagram plot of this diode with the Ga_2O_3 barrier layer under reverse bias is shown in Figure 10. In the diagram, the electron affinity(χ) of SiO_2, Si, ZnO, Ga_2O_3, and MgZnO were taken as 0.9 eV [10], 4.0 eV, 4.35 eV, 4.0 eV, and 4.27 eV [39], respectively. The band gap (Eg) of Si was 1.12 eV [39]. The band gap of Ga_2O_3, ZnO, and MgZnO were 4.77 eV, 3.36 eV, and 3.40 eV, as determined from Figures 2 and 3. The conduction band edge energy difference (ΔEc) and valence band edge energy difference (ΔEv) around Ga_2O_3 were, thus, estimated as [13] 0.27 eV and 1.10 eV for MgZnO-Ga_2O_3 interface and 0.35 eV and 1.06 eV for Ga_2O_3-ZnO respectively.

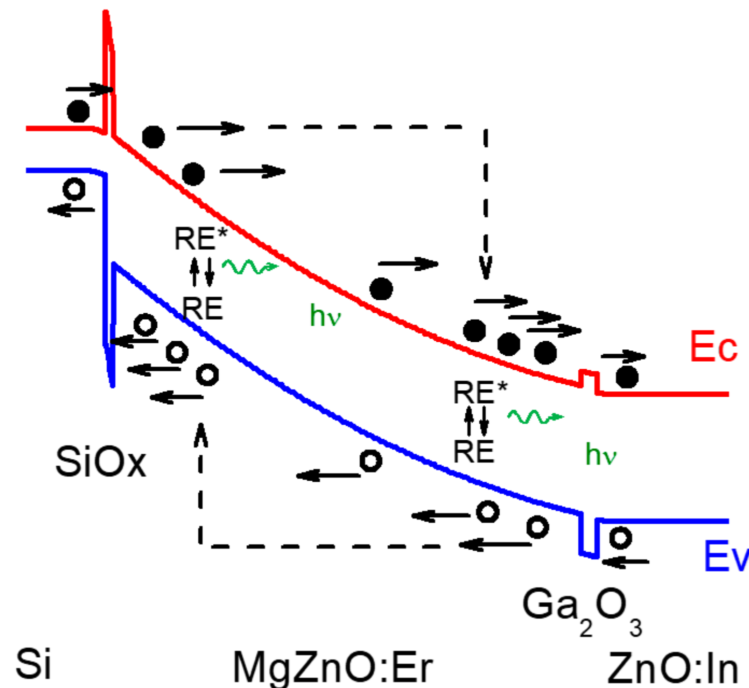

Figure 10. Schematic energy band diagram for the diode with barrier layers under reverse bias.

For the diode operated on the reverse bias before breakdown, electron, and hole emissions through bandgap generation-recombination centers in the depletion region at room temperature. For AT0, the diode with SiOx only, hole generated from the depletion region and minority carrier, i.e., electrons from p-type Si were blocked by the SiOx layer due to its high conduction band discontinuity. With the introduced Ga_2O_3 barrier layers on top of MgZnO:Er, i.e., on the right-hand side in the figure, the low energy electron in the depletion region was blocked, and the current before light emission could be further reduced. This illustrates the dark current reduction for samples AT1 and AT3 with the increased Ga_2O_3 thickness to 4.9 nm. For sample AT7, the increased dark current reveals the increased defect states in this structure, and a high turn-on current for light emission is needed. For the diode operated in the breakdown condition, the electrons and holes accelerated in the opposite direction gain sufficient high energy to excite Er ion to an excited state (Er*) by impact excitation (Er→Er*). In the following relaxation process after excitation, carriers at excited $^2H_{11/2}$ state to $^4I_{15/2}$ state results in one green light emission with a wavelength around 533 nm, and carriers at excited $^4S_{3/2}$ state to $^4I_{15/2}$ state results in the other green light emission with a wavelength around 553 nm (Er*→Er). The high energy carriers make the main contribution to the impact excitation energy transformation and current measured. The introduced Ga_2O_3 served as a barrier layer for blocking low-energy carriers. This causes the reduced turn-on current and steep light intensity to increase with the increase in injection current. For the G_2O_3 barrier layer in the diode structure, carriers with insufficient energy were blocked. This reduced the turn-on current before light emission and improved the luminescent property by effective high-energy carrier injection.

On the other hand, reduced crystalline by the increasing diode ideality and increased series resistance also formed with the increased G_2O_3 layer thickness. This crystalline reduction may be due to Ga_2O_3 thickness and the switching procedures in the deposition procedure. Optimized Ga_2O_3 thickness of 4.9 nm for sample AT3 presents a small turn-on current and high carrier injection-luminescent behavior. For sample AT7 with further thick Ga_2O_3, reduced crystalline by increased dark current and enhanced series resistance degrades the diode electrical and luminescence properties.

4. Conclusions

In conclusion, light-emitting diodes with MgZnO:Er/Ga_2O_3 heterostructures were fabricated by the non-vacuumed spray pyrolysis method. The effect of Ga_2O_3 thickness on the diode's electrical and optoelectrical properties was studied. With increased Ga_2O_3 thickness, a great increase in diode series resistance was characterized under the forward bias condition. The green emissions correspond to Er ion excited $2H_{11/2}$ state and $4S_{3/2}$ state to ground $4I_{15/2}$ state were characterized for the diode with and without Ga_2O_3 barrier layer under the reverse biased condition at room temperature. The Ga_2O_3 on top of MgZnO:Er serves as a barrier layer for blocking carriers and takes effect on the turn-on current and light emission. The reduced turn-on current for light emission and enhanced luminescent characters due to efficient high energy carrier generation were achieved for the diode with Ga_2O_3 thickness around 4.9 nm. For the diode with further thick Ga_2O_3, the degraded diode performance, which was due to the arisen mixed interface defect states, was characterized. The effect of Ga_2O_3 thickness on the diode performance was discussed and realized. The introduced Ga_2O_3 on top of the luminescence host shows an effective factor for improved performance for the rare earth-doped optoelectronic device.

Author Contributions: Conceptualization, W.-H.L. and C.-J.H.; methodology, S.-W.Y., W.-H.L.; software, M.-C.S.; validation, S.-W.Y., S.-Y.C.; formal analysis, M.-C.S., S.-W.Y.; investigation, S.-W.Y., W.-H.L.; resources, S.-Y.C.; data curation, S.-W.Y., W.-H.L.; writing—original draft preparation, S.-W.Y., W.-H.L.; writing—review and editing, S.-Y.C., M.-C.S., W.-H.L.; visualization, S.-Y.C., C.-J.H.; supervision, C.-J.H.; project administration, W.-H.L.; funding acquisition, W.-H.L. All authors have read and agreed to the published version of the manuscript.

Funding: The authors sincerely appreciate the financial support from the National Science and Technology Council, Taiwan, China.

Institutional Review Board Statement: Not applicable.

Informed Consent Statement: Not applicable.

Data Availability Statement: Not applicable.

Acknowledgments: The authors wish to acknowledge the support from the National Science and Technology Council, Taiwan, China (111–2221–E-390–007–). The authors also thank the staff at the National Sun Yat-sen University for assistance with XPS (ESCA) experiments.

Conflicts of Interest: The authors declare no conflict of interest.

References

1. Kandpal, K.; Gupta, N.; Singh, J.; Shekhar, C. Study of ZnO/BST interface for thin-film transistor (TFT) applications. *Surfaces Interfaces* **2021**, *23*, 100996. [CrossRef]
2. Mazandarani, H.R.; Ghafary, B.; Alam, S.N. Optimization of UVB photodiode based on ZnO nanorod arrays grown via the hydrothermal process. *Opt. Mater.* **2022**, *126*, 112047. [CrossRef]
3. Ali, A.T.; Maryam, W.; Huang, Y.W.; Hsu, H.C.; Ahmed, N.M.; Zainal, N.; Hassan, H.A.; Dheyab, M.A. UV random laser in aluminum-doped ZnO nanorods. *J. Opt. Soc. Am. B* **2021**, *38*, C69–C77. [CrossRef]
4. Chen, S.; Zhan, T.; Pan, X.; He, H.; Huang, J.; Lu, B.; Ye, Z. UV electroluminescence emissions from high-quality ZnO/ZnMgO multiple quantum well active layer light-emitting diodes. *RSC Adv.* **2021**, *11*, 38949–38955. [CrossRef] [PubMed]
5. Iwan, S.; Bambang, S.; Zhao, J.L.; Tan, S.T.; Fan, H.M.; Sun, L.; Zhang, S.; Ryu, H.H.; Sun, X.W. Green electroluminescence from an n-ZnO: Er/p-Si heterostructured light-emitting diode. *Physics B* **2012**, *407*, 2721–2724. [CrossRef]

6. Chen, C.A.; Hsu, Y.T.; Lan, W.H.; Huang, K.F.; Chang, K.J.; Wang, M.C.; Huang, C.J. On the Nitrogen Doping in Erbium and Nitrogen Codoped Magnesium Zinc Oxide Diode by Spray Pyrolysis. *Crystals* **2020**, *10*, 34. [CrossRef]
7. Zubia, J.; Arrue, J. Plastic Optical Fibers: An Introduction to Their Technological Processes and Applications. *Opt. Fiber Technol.* **2001**, *7*, 101–140. [CrossRef]
8. Kuo, Y.K.; Wang, T.H.; Chang, J.Y.; Chen, J.D. Slightly-Doped Step-Like Electron-Blocking Layer in InGaN Light-Emitting Diodes. *IEEE Photonics Technol. Lett.* **2012**, *24*, 1506–1508. [CrossRef]
9. Hadouchi, W.; Rousset, J.; Tondelier, D.; Geffroy, B.; Bonnassieux, Y. Zinc oxide as a hole blocking layer for perovskite solar cells deposited in atmospheric conditions. *RSC Adv.* **2016**, *6*, 67715. [CrossRef]
10. Chen, J.; Zhu, W.; Gao, Y.; Yang, D.; Ma, X. Electroluminescence from light-emitting devices based on erbium-doped ZnO/n-Si heterostructures: Enhancement effect of fluorine co-doping. *Opt. Express* **2019**, *27*, 30919. [CrossRef]
11. You, J.B.; Zhang, X.W.; Zhang, S.G.; Wang, J.X.; Yin, Z.G.; Tan, H.R.; Zhang, W.J.; Chu, P.K.; Cui, B.; Wowchak, A.M.; et al. Improved electroluminescence from n-ZnO/AlN/p-GaN heterojunction light-emitting diodes. *Appl. Phys. Lett.* **2010**, *96*, 201102. [CrossRef]
12. Nakahara, K.; Akasaka, S.; Yuji, H.; Tamura, K.; Fujii, T.; Nishimoto, Y.; Takamizu, D.; Sasaki, A.; Tanabe, T.; Takasu, H.; et al. Nitrogen doped MgxZn1−xO/ZnO single heterostructure ultraviolet light-emitting diodes on ZnO substrates. *Appl. Phys. Lett.* **2010**, *97*, 013501. [CrossRef]
13. Liu, Y.; Liang, H.; Xia, X.; Shen, R.; Liu, Y.; Bian, J.; Du, G. Introducing Ga_2O_3 thin films as novel electron blocking layer to ZnO/p-GaN heterojunction LED. *Appl. Phys. B* **2012**, *109*, 605–609. [CrossRef]
14. Zhang, J.; Shi, J.; Qi, D.C.; Chen, L.; Zhang, K.H.L. Recent progress on the electronic structure, defect, and doping properties of Ga_2O_3. *APL Mater.* **2020**, *8*, 020906. [CrossRef]
15. Choi, Y.S.; Kang, J.W.; Kim, B.H.; Na, D.K.; Lee, S.J.; Park, S.J. Improved electroluminescence from ZnO light-emitting diodes by p-type MgZnO electron blocking layer. *Opt. Express* **2013**, *21*, 11698–11704. [CrossRef]
16. Hsu, Y.T.; Lee, C.C.; Lan, W.H.; Huang, K.F.; Chang, K.J.; Lin, J.C.; Lee, S.Y.; Lin, W.J.; Wang, M.C.; Huang, C.J. Thickness Study of Er-Doped Magnesium Zinc Oxide Diode by Spray Pyrolysis. *Crystals* **2018**, *8*, 454. [CrossRef]
17. Li, X.; Liu, D.; Mo, X.; Li, K. Nanorod β-Ga_2O_3 semiconductor modified activated carbon as catalyst for improving power generation of microbial fuel cell. *J. Solid State Electrochem.* **2019**, *23*, 2843–2852. [CrossRef]
18. Huang, C.; Mu, W.; Zhou, H.; Zhu, Y.; Xu, X.; Jia, Z.; Zheng, L.; Tao, X. Effect of OH on chemical mechanical polishing of β-Ga_2O_3 (100) substrate using an alkaline slurry. *RSC Adv.* **2018**, *8*, 6544–6550. [CrossRef]
19. Jiao, S.; Lu, H.; Wang, X.; Nie, Y.; Wang, D.; Gao, S.; Wang, J. The Structural and Photoelectrical Properties of Gallium Oxide Thin Film Grown by Radio Frequency Magnetron Sputtering. *J. Solid State Sci. Technol.* **2019**, *8*, Q3086–Q3090. [CrossRef]
20. Girija, K.; Thirumalairajan, S.; Mastelaro, V.R.; Mangalaraj, D. Photocatalytic degradation of organic pollutants by shape selective synthesis of β-Ga_2O_3 microspheres constituted by nanospheres for environmental remediation. *J. Mater. Chem. A* **2014**, *3*, 2617–2627. [CrossRef]
21. Rodriguez, C.I.M.; Alvarez, M.A.L.; Rivera, J.d.J.F.; Arizaga, G.G.C.; Michel, C.R. α-Ga_2O_3 as a Photocatalyst in the Degradation of Malachite Green. *ECS J. Solid State Sci. Technol.* **2019**, *8*, Q3180–Q3186. [CrossRef]
22. Hinkle, C.L.; Milojevic, M.; Brennan, B.; Sonnet, A.M.; Aguirre-Tostado, F.S.; Hughes, G.J.; Vogel, E.M.; Wallace, R.M. Detection of Ga suboxides and their impact on III-V passivation and Fermilevel pinning. *Appl. Phys. Lett.* **2009**, *94*, 162101. [CrossRef]
23. Usseinov, A.; Koishybayeva, Z.; Platonenko, A.; Pankratov, V.; Suchikova, Y.; Akilbekov, A.; Zdorovets, M.; Purans, J.; Popov, A.I. Vacancy Defects in Ga_2O_3: First-Principles Calculations of Electronic Structure. *Materials* **2021**, *14*, 7384. [CrossRef] [PubMed]
24. Swallow, J.E.N.; Vorwerk, C.; Mazzolini, P.; Vogt, P.; Bierwagen, O.; Karg, A.; Eickhoff, M.; Schörmann, J.; Wagner, M.R.; Roberts, J.W.; et al. Influence of Polymorphism on the Electronic Structure of Ga_2O_3. *Chem. Mater.* **2020**, *32*, 8460. [CrossRef]
25. Tian, R.; Pan, M.; Sai, Q.; Zhang, L.; Qi, H.; Mohamed, H.F. Crucial Role of Oxygen Vacancies in Scintillation and Optical Properties of Undoped and Al-Doped-Ga_2O_3 Single Crystals. *Crystals* **2022**, *12*, 429. [CrossRef]
26. Lee, B.J.; Jo, S.I.; Jeong, G.H. Synthesis of ZnO Nanomaterials Using Low-Cost Compressed Air as Microwave Plasma Gas at Atmospheric Pressure. *Nanomaterials* **2019**, *9*, 942. [CrossRef]
27. Hsu, H.C.; Hsieh, W.F. Excitonic polaron and phonon assisted photoluminescence of ZnO nanowires. *Solid State Commun.* **2004**, *131*, 371–375. [CrossRef]
28. He, H.; Wang, Y.; Wang, J.; Ye, Z. Extraction of the surface trap level from photoluminescence: A case study of ZnO nanostructures. *Phys. Chem. Chem. Phys.* **2011**, *13*, 14902. [CrossRef] [PubMed]
29. Hang, D.R.; Islam, S.E.; Sharma, K.H.; Kuo, S.W.; Zhang, C.Z.; Wang, J.J. Annealing effects on the optical and morphological properties of ZnO nanorods on AZO substrate by using aqueous solution method at low temperature. *Nanoscale Res. Lett.* **2014**, *9*, 632. [CrossRef]
30. Bandopadhyay, K.; Mitra, J. Zn interstitials and O vacancies responsible for ntype ZnO: What do the emission spectra reveal? *RSC Adv.* **2015**, *5*, 23540. [CrossRef]
31. Willander, M.; Nur, O.; Sadaf, J.R.; Qadir, M.I.; Zaman, S.; Zainelabdin, A.; Bano, N.; Hussain, I. Luminescence from Zinc Oxide Nanostructures and Polymers and their Hybrid Devices. *Materials* **2010**, *3*, 2643. [CrossRef]
32. Anjum, A.; Ahmed, R.; Umar, Z.A.; Azzam, S.; Hussain, T.; Sarwar, M.N.; Baig, M.A. Structure and defects-related optical properties of highly (002)-oriented zinc oxide thin films. *Physica B* **2022**, *644*, 414195. [CrossRef]

33. Vempati, S.; Mitra, J.; Dawson, P. One-step synthesis of ZnO nanosheets: A blue-white fluorophore. *Nanoscale Res. Lett.* **2012**, *7*, 470. Available online: https://www.nanoscalereslett.com/content/7/1/470 (accessed on 21 November 2022). [CrossRef] [PubMed]
34. Shan, F.K.; Kim, B.I.; Liu, G.X.; Liu, Z.F.; Sohn, J.Y.; Lee, W.J.; Shin, B.C.; Yu, Y.S. Blueshift of near band edge emission in Mg doped ZnO thin films and aging. *J. Appl. Phys.* **2004**, *95*, 4772–4776. [CrossRef]
35. Naik, S.S.; Reddy, V.R. Temperature dependency and current transport mechanisms of Pd/V/n-type InP schottky rectifiers. *Adv. Mat. Lett.* **2012**, *3*, 188–196. [CrossRef]
36. Breitenstein, O.; Altermatt, P.; Ramspeck, K.; Green, M.A.; Zhao, J.; Schenk, A. Interpretation of the Commonly Observed I-V Characteristics of C-SI Cells Having Ideality Factor Larger than Two. In Proceedings of the 2006 IEEE 4th World Conference on Photovoltaic Energy Conference, Waikoloa, HI, USA, 7–12 May 2006; pp. 879–884. [CrossRef]
37. Pollnau, M.; Gamelin, D.R.; Luthi, S.R.; Gudel, H.U.; Hehlen, M.P. Power dependence of upconversion luminescence in lanthanide and transition-metal-ion systems. *Phys. Rev. B* **2000**, *61*, 3337–3346. [CrossRef]
38. Brandão-Silva, A.C.; Gomes, M.A.; Novais, S.M.V.; Macedo, Z.S.; Avila, J.F.M.; Rodrigues, J.J.; Alencar, M.A.R.C. Size influence on temperature sensing of erbium-doped yttrium oxide nanocrystals exploiting thermally coupled and uncoupled levels' pairs. *J. Alloys Compd.* **2018**, *731*, 478–488. [CrossRef]
39. Zhang, W.; Tang, N. Comparative study of ZnMgO/GaAs and ZnMgO/Si solar cells. *Mater. Res. Express* **2020**, *7*, 105903. [CrossRef]

Disclaimer/Publisher's Note: The statements, opinions and data contained in all publications are solely those of the individual author(s) and contributor(s) and not of MDPI and/or the editor(s). MDPI and/or the editor(s) disclaim responsibility for any injury to people or property resulting from any ideas, methods, instructions or products referred to in the content.